

CHAPTER 5
IONOTHERMAL SYNTHESIS AND CRYSTAL STRUCTURES
OF NEW d^{10} BLUE LUMINESCENT METAL–
ORGANIC MATERIALS

Continuous growth of interest in MOMs stems not only from potential applications in selective gas storage/adsorption, catalysis, and luminescence [1–5], but also from their intriguing structures and topologies [5–7]. Although the coordination of ligands to central metal ions and the assembly of the derived structural building motifs in solid state can be accomplished in numerous ways, one of the most pronounced route is solvo(hydro)thermal technique [2, 3, 8]. The use of water which may lead to the hydrolysis of organic ligands, and the need to dissolve the immiscible metal source and targeted organic template in the same solvent during solvo(hydro)thermal reaction may nonetheless hinder a successful synthesis [9, 10]. Ionothermal technique involving the use of ionic liquid solvents, *e.g.* 1-butyl-3-methylimidazoliumtetrafluoroborate (BMIm-BF₄), 1-butyl-3-methylimidazolium hexafluorophosphate (BMIm-PF₆), 1-ethyl-3-methylimidazolium bis(trifluoromethyl)sulfonylimide (BMIm-Tf₂N) and 1-alkyl-3-methylimidazolium halide (RMIm-X; R = ethyl, propyl and butyl, X = Cl⁻, Br⁻, I⁻), at lower vapor pressures and near-ambient temperatures, has recently emerged as a very promising alternative [10–14]. Properties of the ionic liquids, *e.g.* polarity, high ionic

conductivity and very low vapor pressure, which can be tuned by changing the cationic organic and/or anionic inorganic components [10–16], make them suitable to be solvents for a wide range of precursors. Possibility of the ionic liquids in incorporating into the synthesized MOMs as ligands, charge compensating motifs and even templates of the synthesized frameworks, make them facilitate the additional functions of ionic liquids in the synthesis [10–16]. In fabricating MOMs, dicarboxylate ligands have been extensively investigated as the framework building motifs [7, 17–20], particularly in the Zn–benzenedicarboxylate compounds [18–20]. This is partially due to the promising future in the applications of gas storage of these compounds [5, 18–20]. The synthesized compounds are nonetheless very sensitive to variations in the synthesis, including the water content in the reactions. The use of ionic liquids is therefore very interesting in providing the polar non-aqueous system.

In this chapter, the use of two ionic liquids, *i.e.* 1-ethyl-3-methylimidazolium chloride (EMIm-Cl) and 1-butyl-3-methylimidazolium chloride (BMIm-Cl), as the functional solvents in the syntheses of two new MOMs using 1,4-benzenedicarboxylic acid (H₂BDC) as primary ligands *i.e.* EMIm₂[Zn₃(BDC)₃Cl₂] (**IV**) and BMIm₂[Zn₃(BDC)₃Cl₂] (**V**), is reported. The subtle templating effects of the two ionic liquids on the derived framework structures, supramolecular assemblies and topologies are discussed. Thermogravimetric and photoluminescence properties of **IV** and **V** are described. The investigation on structures and properties of the de-intercalated compounds derived from **IV** and **V** are also included.

5.1 Experimental

5.1.1 Synthesis and characterizations

All chemicals were obtained commercially and used without further purification; $\text{Zn}(\text{NO}_3)_2 \cdot 6\text{H}_2\text{O}$ (Ajax Finechem, 98%), 1,4-benzenedicarboxylic acid (H_2BDC ; $\text{C}_6\text{H}_4(\text{COOH})_2$; BDH, 97%), 1-ethyl-3-methylimidazolium chloride (EMIm-Cl, $\text{C}_6\text{H}_{11}\text{ClN}_2$; Sigma-Aldrich, 99%) and 1-butyl-3-methylimidazolium chloride (BMIm-Cl, $\text{C}_8\text{H}_{15}\text{ClN}_2$; Sigma-Aldrich, 99%).

Single crystals of two isorecticular compounds, *i.e.* EMIm₂[Zn₃(BDC)₃Cl₂] (**IV**) and BMIm₂[Zn₃(BDC)₃Cl₂] (**V**), were synthesized from the reactions between $\text{Zn}(\text{NO}_3)_2 \cdot 6\text{H}_2\text{O}$ (0.7437 g, 2.5 mmol) and H_2BDC (0.0856 g, 0.5 mmol) in EMIm-Cl (1.0000 g, 6.8 mmol) for **IV** and BMIm-Cl (1.0000 g, 5.7 mmol) for **V**. The reactions were performed using a 7.00 cm³ Teflon lined hydrothermal autoclave under an autogeneous pressure generated at 180 °C for 10 days, after which the colorless crystals were obtained. The yielded reaction products are shown to be pure crystals under the optical microscope for both **IV** and **V**. The powder X-ray diffraction data confirmed the purity of the yielded crystal products.

The chemical composition of bulk samples were determined by microanalytical procedures using a Thermo EA1112 Flash CHNS-O Analyzer and the percentage of C, H, and N contents were as follows: $\text{Zn}_3\text{C}_{36}\text{H}_{34}\text{N}_4\text{O}_{12}\text{Cl}_2$ (**IV**). Anal. Calc. (%): C, 44.01; H, 3.46; N, 5.70. Found (%): C, 43.88; H, 3.47; N, 5.82. $\text{Zn}_3\text{C}_{40}\text{H}_{42}\text{N}_4\text{O}_{12}\text{Cl}_2$ (**V**). Anal. Calc. (%): C, 46.25; H, 4.08; N, 5.40. Found (%): C, 46.29; H, 4.12; N, 5.45. Infrared (IR) spectra of the ground samples were recorded using a Bruker Tensor 27 FT-IR instrument in the range of 400–4000 cm⁻¹ using KBr

discs (BDH, 98.5%). Raman spectra were collected in the range of 100–4000 cm^{-1} using a JOBIN YVON HORIBA T64000 spectrophotometer, operated with 35mW solid state laser excitation source. UV–Vis spectra were collected on the suspension of the ground samples in deionized water at room temperature from 200 nm to 800 nm using Perkin Elmer UV LAMDA 25 spectrophotometer. Photoluminescence spectra were collected at room temperature on the ground crystals using an Avantes Multichannel spectrometer with the Ocean Optics LED 255 nm excitation source. Thermogravimetric analyses were performed on a SDT Q600 V20.9 Build 20 in the temperature range 293–1173 K with a heating rate 10 $\text{K}\cdot\text{min}^{-1}$ in a nitrogen gas flow. Powder X–ray diffraction experiments were conducted by using a Rigaku MiniFlex II desktop X–ray diffractometer operated with Cu $K\alpha$ radiation ($\lambda = 1.540562 \text{ \AA}$).

5.1.2 Single crystal structure determination

Intensity data sets of **IV** and **V** were collected on single crystals of sizes $1.00 \times 0.90 \times 0.40$ and $0.70 \times 0.38 \times 0.20 \text{ mm}^3$, respectively, at 293(2) K using a Bruker APEX–II CCD diffractometer operated with Mo $K\alpha$ radiation ($\lambda = 0.71073 \text{ \AA}$). Data reduction and adsorption correction were performed with the SAINT and SADABS software packages [21, 22]. The structures were solved by direct methods and full–matrix least squares refinements were carried out against F^2 for all data with SHELX–97 program [23] *via* the WinGX program interface [24]. Due to the twinning problem in the case of **V**, the HKLF5 was employed. The file was generated using two twin components and a twin matrix (1 0.025 0.033, 0 -1 0, 0 0 -1) which was determined by Rotax [25]. The twin fraction was refined to the final value of

0.782:0.218, which resulted in the improvement of the R and R_w values from 0.0769 and 0.2278 to 0.0590 and 0.1635, respectively. Approximately 6% of the data was omitted. The crystallographic data and refinement details for **IV** and **V** are summarized in Table 5.1. The refined atomic coordinates and equivalent isotropic displacement parameters data of **IV** and **V** are provided in Table 5.2–5.3. The selected bond distances about the metal centers for the reported compounds are listed in Table 5.4–5.5.

Table 5.1 Crystal and experimental data for **IV** and **V**.

Identification code	IV	V
Empirical formula	$C_{36}H_{34}Cl_2N_4O_{12}Zn_3$	$C_{40}H_{42}Cl_2N_4O_{12}Zn_3$
Formula weight	981.68	1037.79
Crystal system	Monoclinic	Triclinic
Space group	$P2_1/n$	$P\bar{1}$
a (Å)	12.7455(8)	9.8465(16)
b (Å)	9.5044(6)	12.963(2)
c (Å)	18.1128(12)	18.047(3)
α (°)	90	109.695(4)
β (°)	108.132(3)	91.397(5)
γ (°)	90	90.383(4)
V (Å ³)	2085.2(2)	2167.8(6)
Z	2	2
T (K)	293(2)	293(2)
$\rho_{\text{calc.}}$ (g·cm ⁻³)	1.564	1.590
μ (Mo- $K\alpha$, mm ⁻¹)	1.903	1.835
θ range (°)	2.45–30.61	1.20–29.13
λ (Mo $K\alpha$) (Å)	0.71073	0.71073
Reflection collected	15035	15698
Unique reflections	6028	15698
Number of parameters	259	556
Number of restraints	0	111
R , R_w ($I > 2\sigma(I)$)	0.1098, 0.2206	0.0590, 0.1635
R , R_w (all data)	0.1613, 0.2546	0.0776, 0.1781
Goodness of fit	1.205	1.046

Table 5.2 Atomic coordinates and equivalent isotropic displacement parameters for **IV**.

	<i>x</i>	<i>y</i>	<i>z</i>	<i>U</i> (eq) (Å ²)
Zn1	0.79678(7)	-0.04027(10)	0.07314(5)	0.0236(2)
Zn2	1	0	0	0.0214(3)
Cl1	0.6619(2)	-0.1517(4)	0.10157(18)	0.0594(8)
O1	0.8889(5)	0.0709(7)	0.1608(3)	0.0337(13)
O2	1.0264(5)	0.0834(7)	0.1090(3)	0.0379(14)
O3	0.7238(5)	0.0831(7)	-0.0147(3)	0.0388(15)
O4	0.8704(5)	0.1268(7)	-0.0525(4)	0.0390(15)
O5	0.8905(5)	-0.1551(6)	0.0286(3)	0.0288(11)
O6	0.9406(7)	-0.2646(7)	0.1426(4)	0.0464(17)
N1	0.8020(11)	-0.0943(15)	0.3308(8)	0.081(3)
N2	0.9403(11)	-0.2318(14)	0.3537(7)	0.079(3)
C1	0.9875(6)	0.1011(9)	0.1630(4)	0.0277(15)
C2	1.0603(6)	0.1660(9)	0.2355(4)	0.0296(16)
C3	1.0180(6)	0.2144(11)	0.2924(5)	0.037(2)
C4	1.0866(7)	0.2762(11)	0.3584(5)	0.040(2)
C5	1.1982(6)	0.2917(9)	0.3695(4)	0.0292(16)
C6	1.2404(7)	0.2407(12)	0.3129(5)	0.042(2)
C7	1.1716(7)	0.1786(12)	0.2470(5)	0.044(2)
C8	0.7707(6)	0.1334(9)	-0.0602(4)	0.0282(15)
C9	0.9332(7)	-0.2612(8)	0.0730(5)	0.0319(16)
C10	0.9682(7)	-0.3846(8)	0.0353(5)	0.0299(16)
C11	0.9429(8)	-0.3907(9)	-0.0454(5)	0.039(2)
C12	1.0257(9)	-0.4948(9)	0.0803(5)	0.040(2)
C13	0.8163(17)	-0.148(3)	0.4003(12)	0.120(8)
C14	0.9029(18)	-0.235(2)	0.4145(10)	0.109(7)
C15	0.8787(13)	-0.1445(17)	0.3025(8)	0.076(4)
C16	1.0367(19)	-0.308(3)	0.3474(15)	0.153(11)
C17	1.136(2)	-0.232(4)	0.3782(16)	0.198(17)
C18	0.7126(17)	0.005(2)	0.2956(13)	0.139(9)

Table 5.3 Atomic coordinates and equivalent isotropic displacement parameters for **V**.

	<i>x</i>	<i>y</i>	<i>z</i>	<i>U</i> (<i>eq</i>) (Å ²)
Zn1	0.44510(5)	0.18961(4)	0.42035(2)	0.02178(12)
Zn2	0.5	0	0.5	0.02018(15)
Zn3	1.05197(5)	0.69941(4)	0.93137(2)	0.02217(12)
Zn4	1	0.5	1	0.01967(15)
Cl1	0.35103(16)	0.32029(11)	0.38331(8)	0.0511(4)
Cl2	1.15195(15)	0.83341(10)	0.90104(8)	0.0454(3)
O1	0.5708(4)	0.2712(2)	0.50786(16)	0.0337(8)
O2	0.6260(4)	0.1297(2)	0.54585(18)	0.0359(8)
O3	0.9336(3)	0.6136(2)	0.84180(16)	0.0325(7)
O4	0.9172(4)	0.4762(3)	0.88965(16)	0.0396(8)
O5	0.5524(4)	0.0947(2)	0.33408(16)	0.0337(7)
O6	0.5701(4)	-0.0388(3)	0.38659(15)	0.0366(8)
O7	0.3380(3)	0.1039(2)	0.47310(16)	0.0260(6)
O8	0.2256(4)	0.0534(4)	0.35781(19)	0.0523(10)
O9	0.8840(4)	0.6314(2)	1.05412(18)	0.0361(8)
O10	0.9371(3)	0.7783(2)	1.02180(16)	0.0323(7)
O11	1.1611(3)	0.6067(2)	0.97874(16)	0.0257(6)
O12	1.2557(4)	0.5562(3)	0.86155(19)	0.0491(10)
N1	1.2216(7)	0.9840(5)	1.1641(3)	0.0682(15)
N2	1.2977(6)	1.1345(4)	1.1551(3)	0.0571(13)
N3	1.1042(7)	0.7198(5)	0.6777(3)	0.0742(15)
N4	1.2617(6)	0.5985(5)	0.6657(3)	0.0755(15)
C1	0.6283(5)	0.2296(3)	0.5546(2)	0.0248(9)
C2	0.7027(5)	0.3048(3)	0.6259(2)	0.0306(10)
C3	0.7569(7)	0.2645(4)	0.6805(3)	0.0520(17)
C4	0.8200(7)	0.3335(4)	0.7492(3)	0.0556(17)
C5	0.8322(5)	0.4445(3)	0.7620(2)	0.0300(10)
C6	0.7774(5)	0.4855(3)	0.7060(2)	0.0340(11)
C7	0.7136(5)	0.4164(3)	0.6381(2)	0.0331(11)
C8	0.9001(5)	0.5166(3)	0.8374(2)	0.0287(9)
C9	0.5902(4)	0.0015(3)	0.3343(2)	0.0261(9)
C10	0.6652(5)	-0.0669(3)	0.2637(2)	0.0291(10)
C11	0.7173(5)	-0.0226(4)	0.2102(2)	0.0332(10)

Table 5.3 Atomic coordinates and equivalent isotropic displacement parameters for **V**
(continued).

	<i>x</i>	<i>y</i>	<i>z</i>	<i>U</i> (<i>eq</i>) (Å ²)
C12	0.2329(5)	0.0621(4)	0.4280(3)	0.0299(10)
C13	0.1136(5)	0.0274(4)	0.4655(2)	0.0302(10)
C14	0.1151(5)	0.0444(4)	0.5453(3)	0.0375(11)
C15	-0.0018(5)	-0.0163(4)	0.4205(3)	0.0369(11)
C16	0.8814(4)	0.7316(3)	1.0645(2)	0.0243(9)
C17	0.8056(5)	0.8030(3)	1.1343(2)	0.0250(9)
C18	0.7528(6)	0.7589(4)	1.1873(3)	0.0408(13)
C19	0.6839(6)	0.8218(4)	1.2513(3)	0.0412(13)
C20	0.7874(5)	0.9141(3)	1.1469(2)	0.0294(10)
C21	1.2598(5)	0.5639(4)	0.9312(3)	0.0300(10)
C22	1.3821(5)	0.5291(4)	0.9670(2)	0.0288(9)
C23	1.4892(5)	0.4820(4)	0.9197(3)	0.0377(11)
C24	1.3924(5)	0.5462(4)	1.0474(3)	0.0356(11)
C25	1.3139(8)	1.0673(6)	1.1933(3)	0.0665(18)
C26	1.1487(8)	1.0028(6)	1.1070(4)	0.078(2)
C27	1.1975(7)	1.0975(5)	1.0990(4)	0.0615(16)
C28	1.2181(11)	0.8878(6)	1.1871(5)	0.108(3)
C29	1.3830(8)	1.2301(6)	1.1663(4)	0.081(2)
C30	1.4847(9)	1.2187(8)	1.1083(4)	0.099(2)
C31	1.4431(10)	1.1880(9)	1.0240(5)	0.120(3)
C32	1.5486(9)	1.1701(7)	0.9612(4)	0.105(3)
C33	1.1579(8)	0.6496(6)	0.7089(4)	0.0755(18)
C34	1.2707(9)	0.6373(7)	0.6038(4)	0.089(2)
C35	1.1745(9)	0.7124(7)	0.6126(5)	0.087(2)
C36	0.9906(9)	0.7893(7)	0.7077(5)	0.105(3)
C37	1.3410(11)	0.5067(8)	0.6761(5)	0.120(4)
C38	1.3056(14)	0.3955(9)	0.6173(8)	0.170(5)
C39	1.1636(16)	0.3584(13)	0.6264(9)	0.198(5)
C40	1.0855(16)	0.3721(14)	0.5636(8)	0.223(7)

Table 5.4 Selected geometric parameters for **IV**.

<i>Bond distances (Å)</i>			
Zn1–O1	1.963(5)	Zn2–O2	2.055(5)
Zn1–O3	1.962(5)	Zn2–O4	2.027(5)
Zn1–O5	1.967(5)	Zn2–O5	2.200(5)
Zn1–Cl1	2.212(2)		
<i>Bond angles (°)</i>			
O3–Zn1–O1	110.3(3)	O5–Zn1–Cl1	116.42(19)
O3–Zn1–O5	101.2(2)	O2–Zn2–O5	87.6(2)
O1–Zn1–O5	110.1(2)	O4–Zn2–O2	95.0(3)
O3–Zn1–Cl1	105.5(2)	O4–Zn2–O5	91.4(2)
O1–Zn1–Cl1	112.47(19)		

Table 5.5 Selected geometric parameters for **V**.

<i>Bond distances (Å)</i>			
Zn1–O1	1.976(3)	Zn3–O3	1.972(3)
Zn1–O5	1.965(3)	Zn3–O10	1.992(3)
Zn1–O7	2.000(3)	Zn3–O11	1.999(3)
Zn1–Cl1	2.2199(13)	Zn3–Cl2	2.2205(13)
Zn2–O2	2.009(3)	Zn4–O4	2.057(3)
Zn2–O6	2.073(3)	Zn4–O9	2.030(3)
Zn2–O7	2.242(3)	Zn4–O11	2.221(3)
<i>Bond angles (°)</i>			
O1–Zn1–O5	108.52(14)	O4–Zn4–O9	94.45(14)
O1–Zn1–O7	100.15(12)	O4–Zn4–O11	89.84(12)
O5–Zn1–O7	112.19(12)	O9–Zn4–O11	91.53(12)
O1–Zn1–Cl1	103.51(10)	O3–Zn3–O10	109.12(14)
O5–Zn1–Cl1	109.38(10)	O3–Zn3–O11	113.41(12)
O7–Zn1–Cl1	121.59(10)	O10–Zn3–O11	100.41(12)
O2–Zn2–O6	94.65(14)	O3–Zn3–Cl2	108.78(10)
O2–Zn2–O7	92.09(12)	O10–Zn3–Cl2	103.66(10)
O6–Zn2–O7	90.27(11)	O11–Zn3–Cl2	120.17(9)

5.1.3 Structure and property of the de-intercalated samples

In order to study stability and properties of the de-intercalated samples of **IV** and **V**, the crystals were dispersed in deionized water using a general ultrasonic bath at 70(±5) °C. The fine white powders were obtained after 60 mins for both compounds, and were characterized by elemental analyses, powder X-ray diffraction, IR and Raman spectroscopies, thermogravimetric analyses, UV-Vis and photoluminescence spectroscopies. The powder samples obtained from compounds **IV** and **V** will hereafter be denoted as **IV-L** and **V-L**, respectively.

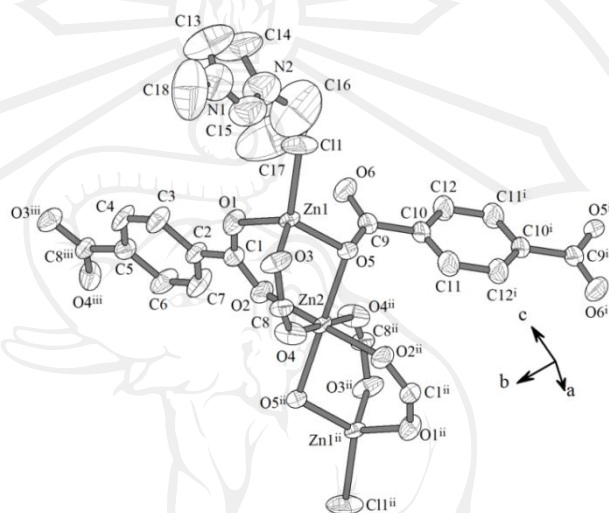
5.2 Results and discussion

5.2.1 Crystal structures description

Compounds **IV** and **V** feature the same two-dimensional $[\text{Zn}_3(\text{BDC})_3\text{Cl}_2]^{2-}$ anionic layered structure which is intercalated and charge-neutralized by two different extraframework cations, *i.e.* EMIm⁺ (**I**) and BMIm⁺ (**II**). As depicted in Fig. 5.1a, the asymmetric unit of **IV** contains twenty-nine non-hydrogen atoms comprising two crystallographically independent Zn ions (Zn1 and Zn2), one and a half molecules of BDC²⁻, and one each of Cl⁻ and EMIm⁺ ions. The two independent Zn ions in **IV** adopt different coordination environments. The four-coordinated Zn1 ion shows a tetrahedral environment fulfilled by an apical Cl⁻ anion and three basal O atoms (O1, O3, O5). The six-coordinated Zn2 on the other hand shows a distorted octahedral geometry completed by two equivalent apical O atoms (O5) and two pairs of equivalent O atoms (O2 and O4) in a basal plane. The tetrahedral and octahedral units of Zn ions notably share the common vertex (O5). Bond distances for the Zn-O

of the tetrahedral Zn1 (1.962(5)–1.967(5) Å) are distributed in a shorter range than those for the octahedral Zn2 (2.027(5)–2.200(5) Å). The observed difference is in MOMs comprising good agreement with those reported for relevant compounds [26–29].

(a)



(b)

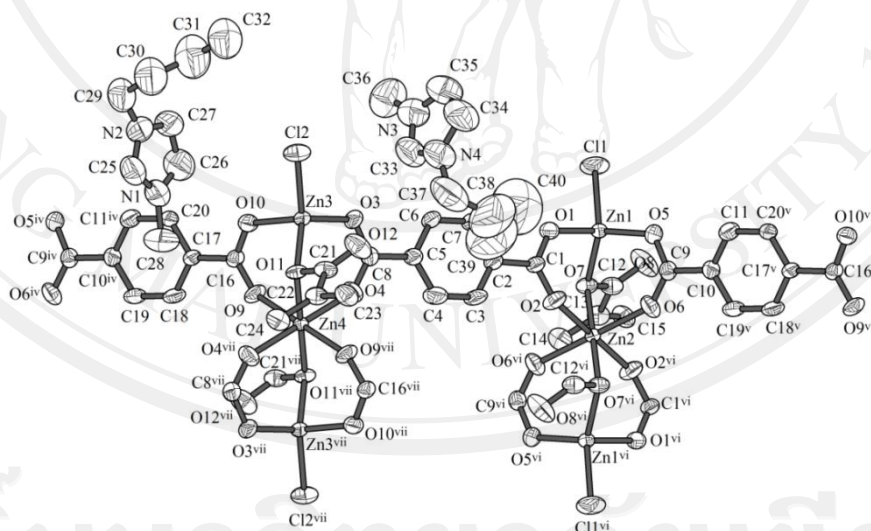


Fig. 5.1 Views of the extended asymmetric units of (a) **IV** and (b) **V**, showing the tetrahedral–octahedral–tetrahedral trimers. Thermal ellipsoids are shown with 60% probability, and hydrogen atoms are omitted for clarity. Symmetry codes: (i) $2 - x, -1 - y, -z$; (ii) $2 - x, -y, -z$; (iii) $\frac{1}{2} + x, \frac{1}{2} - y, \frac{1}{2} + z$; (iv) $x, 1 + y, 1 + z$; (v) $x, -1 + y, -1 + z$; (vi) $1 - x, -y, 1 - z$; (vii) $2 - x, 1 - y, 2 - z$.

The Zn1 and Zn2 ions are linked through two $\mu_2\text{-}\eta^1\text{:}\eta^1$ carboxylato bridges (O1–C1–O2 and O3–C8–O4) of two equivalent BDC²⁻ ligands, and an $\mu_2\text{-}\eta^2\text{:}\eta^0$ carboxylato bridge (O5 of O5–C9–O6) of the other BDC²⁻. Due to the inversion on the octahedral Zn2 ion, which is located on the specific Wyckoff 2a site, the corner-sharing tetrahedra–octahedra–tetrahedra trimer of chemical composition [Zn₃O₂(OCO)₄Cl₂] is formed. If coordination mode of each carboxylato bridge is taken into account, the trimer can be presented as [Zn₃($\mu_2\text{-}\eta^2\text{:}\eta^0\text{-OCO}$)₂($\mu_2\text{-}\eta^1\text{:}\eta^1\text{-OCO}$)₄Cl₂]. This type of trimer is only common in the MOMs comprising Zn and BDC²⁻ ligands, *e.g.* Zn₃(BDC)₃(EtOH)₂, Zn₃(BPDC)₃(DMF)₂·4DMF and Zn₃(BDC)₃(DEF)₂ [26–29]. In **IV**, each [Zn₃(OCO)₆Cl₂] trimer is further connected to the other twelve Zn ions of six neighboring trimers in three different directions; [$\frac{1}{2}$ $\frac{1}{2}$ $\frac{1}{2}$] and [$\frac{1}{2}$ $-\frac{1}{2}$ $\frac{1}{2}$] through two pairs of $\mu_2\text{-}\eta^1\text{:}\eta^1$ carboxylato bridges and [0 1 0] through two equivalent $\mu_2\text{-}\eta^2\text{:}\eta^0$ bridges. This leads to the formation of a two-dimensional anionic sheet of [Zn₃(BDC)₃Cl₂]²⁻ extending in the (1 0 -1) plane, as illustrated in Fig. 5.2a.

In comparison to the structure **IV** which is crystallized in the monoclinic $P2_1/n$, the crystal of **V** crystallized in the triclinic $P\bar{1}$, which is a non-isomorphic subgroup of $P2_1/n$. A decrease in the crystal symmetry can be accounted for by an increase in the flexible hydrocarbon chain length of the ionic liquid medium in the synthesis. In the asymmetric unit of **V**, there are as many as sixty-two non-hydrogen atoms comprising four crystallographically distinct Zn ions, two whole molecules and two halves of the BDC²⁻, and two each of the Cl⁻ and BMIm⁺ ions (Fig. 5.1b).

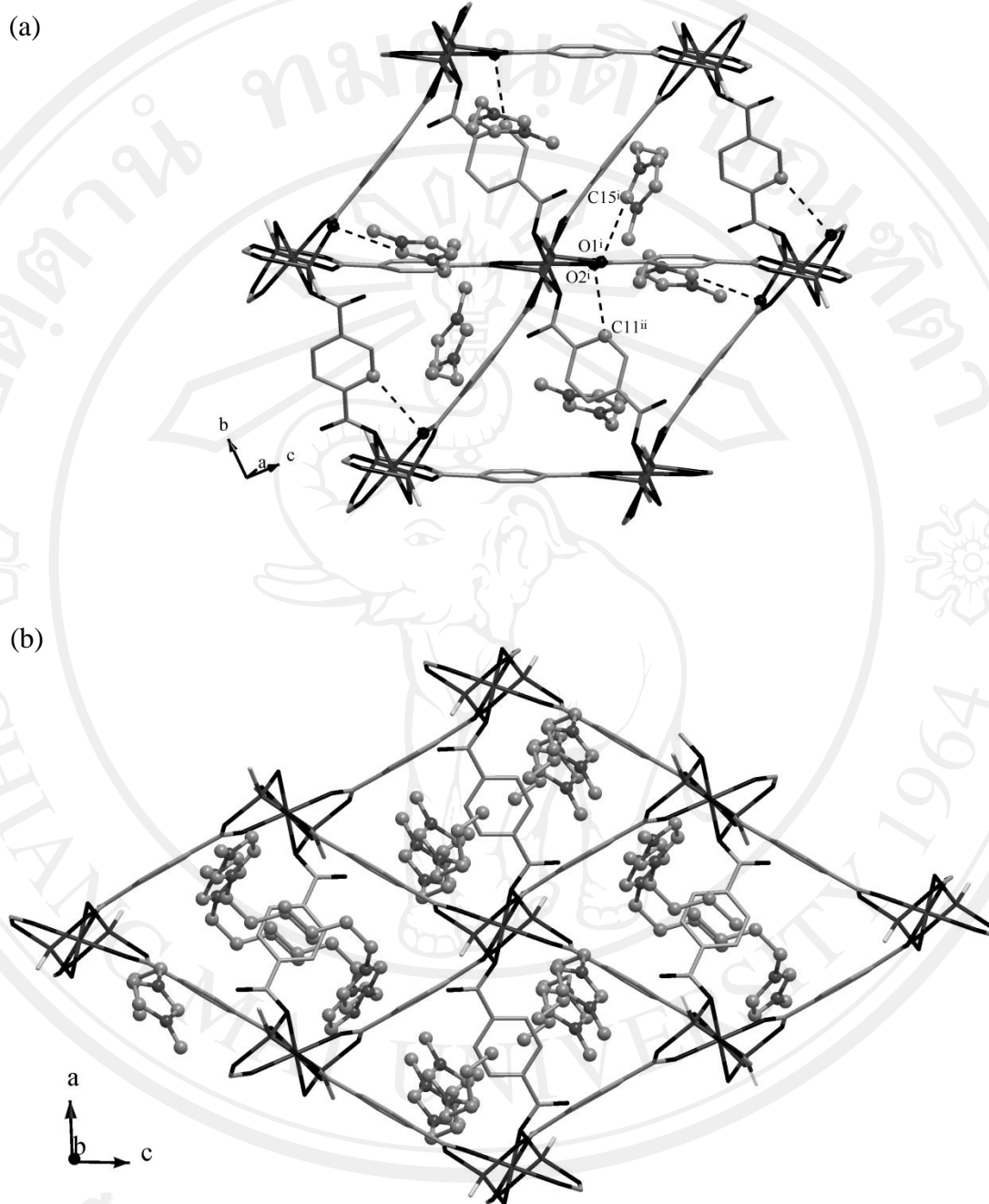


Fig. 5.2 Views of the extended layered structure of (a) **IV** and (b) **V**, showing spatial arrangements of the extraframework cations and C–H···O hydrogen bonding interactions (dotted lines). Symmetry codes: (i) $-\frac{1}{2} + x, \frac{1}{2} - y, \frac{1}{2} + z$; (ii) $\frac{3}{2} - x, \frac{1}{2} + y, \frac{1}{2} - z$.

The Zn ions exhibit a combination of tetrahedral (Zn1 and Zn3) and octahedral (Zn2 and Zn4) geometries with the same tetrahedral–octahedral–tetrahedral arrangement as that present in **IV**. Bond distances for the Zn–O of the tetrahedral and octahedral Zn ions are however varied in slightly larger ranges compared to those of **IV**; 1.965(3)–2.000(3) and 2.009(3)–2.242(3) Å for tetrahedral and octahedral Zn ions, respectively. The four independent Zn ions constitute two crystallographically independent $[\text{Zn}_3(\text{OCO})_6\text{Cl}_2]$ trimers, which are linked by the BDC^{2-} ligands to form an isostructural $[\text{Zn}_3(\text{BDC})_3\text{Cl}_2]^{2-}$ sheet as **IV** (Fig 5.2b). The two–dimensional sheet in **V** extends nonetheless in the (0 1 -1) plane. The common corners in the corner–sharing tetrahedral–octahedral–tetrahedral trimers of **V** are O7 and O11, and the inversion symmetry is located on the octahedral Zn2 and Zn4 ions. The connections of the trimers in **V** occur in also three different directions; [1 1 1] and [0 -1 -1] through four $\mu_2\text{-}\eta^1\text{:}\eta^1$ carboxylato bridges (O1–C1–O2, O3–C8–O4, O5–C9–O6 and O9–C16–O10), and [1 0 0] through two $\mu_2\text{-}\eta^2\text{:}\eta^0$ carboxylato bridges (O7–C12–O8 and O11–C12–O12).

The $[\text{Zn}_3(\text{BDC})_3\text{Cl}_2]^{2-}$ anionic sheets in **IV** and **V** can be simplified to the same (3, 6) uninodal net of triangular grid of the hexagonal lattice (**hxl**) type (Fig. 5.3), with the tetrahedral–octahedral–tetrahedral trimer serving as node. The (3, 6) net is apparently regular among the two–dimensional networks composing of similar trinuclear Zn nodes and dicarboxylato bridges; *e.g.* $[\text{Zn}_3(\text{BDC})_3(\text{H}_2\text{O})_2]\cdot 4\text{DMF}$ [26, 27], $[\text{Zn}_3(\text{BDC})_3(\text{EtOH})_2]$ [26], $[\text{Zn}_3(\text{BDC})_3(\text{H}_2\text{O})_3]\cdot 4\text{DMF}$ [28], $[\text{Zn}_3(\text{BDC})_3(\text{DEF})_2]$ [29], and $[\text{Zn}_3(\text{BPDC})_3(\text{DMF})_2]\cdot 4\text{DMF}$ [29]. Despise being isorecticular, distances measured between the two apical Cl^- ions of the trimer (10.764(5) Å in **IV** and

10.890(3)–10.836(3) Å in **V**) and the two adjacent octahedral Zn ions of the triangular grid (9.5044(6)–10.4543(5) Å in **IV** and 9.847(2)–10.528(1) Å in **V**) suggest a better compact sheet structure in **IV**.

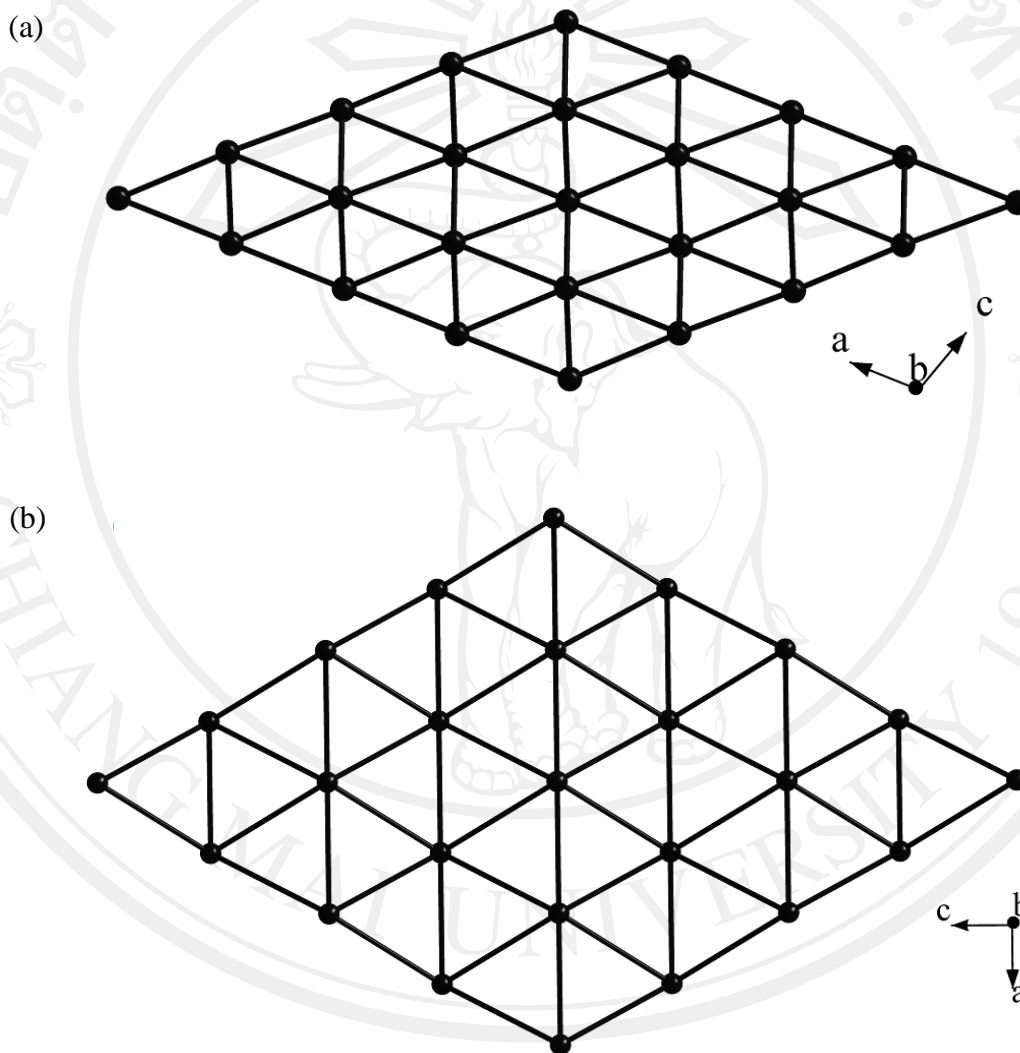


Fig. 5.3 The (3,6) uninodal net of **hxl** topology or triangular grid of the isorecticular (a) **IV** and (b) **V**.

The $[\text{Zn}_3(\text{BDC})_3\text{Cl}_2]^{2-}$ anionic sheets of both **IV** and **V** are stacked in the ABAB fashion, but in two different directions, *i.e.* $[1\ 0\ -1]$ and $[0\ 1\ -1]$ in the cases of

IV and **V**, respectively (Fig. 5.4 and Fig. 5.5). The inter-sheet gallery is intercalated by the positively charged species, *i.e.* EMI⁺ (**IV**) and BMI⁺ (**V**), balancing the negative charges of the $[\text{Zn}_3(\text{BDC})_3\text{Cl}_2]^{2-}$ sheets. Because of a larger size of BMI⁺ cations, the inter-sheet distance of **V** (12.02 Å) is larger than that of **IV** (11.78 Å) where the EMI⁺ cations are present. These values are in excellent agreement with those calculated from the powder X-ray diffraction patterns, *i.e.* 11.86 Å and 12.08 Å for **IV** and **V**, respectively.

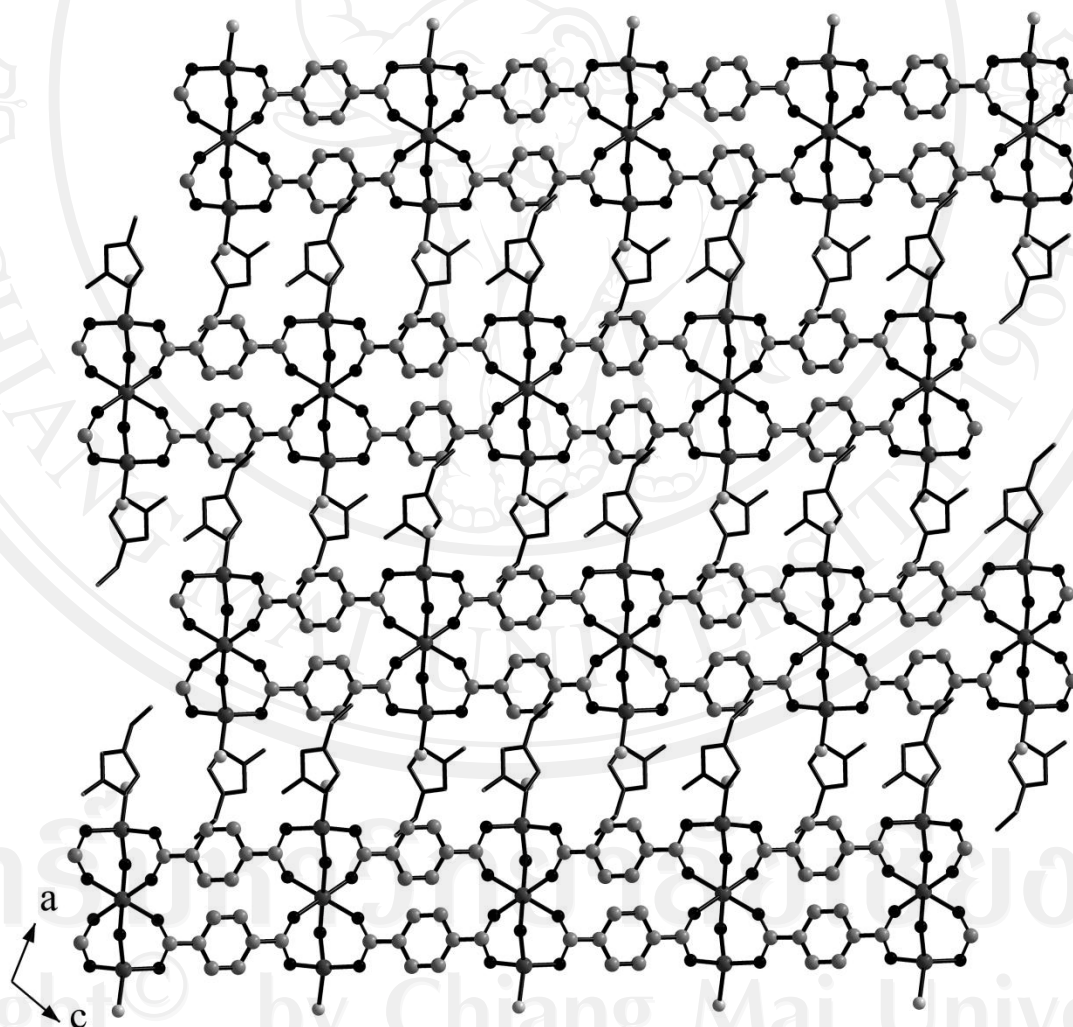


Fig. 5.4 The ABAB stacking of the two-dimensional in **IV**, intercalated by the extraframework EMI⁺ cations.

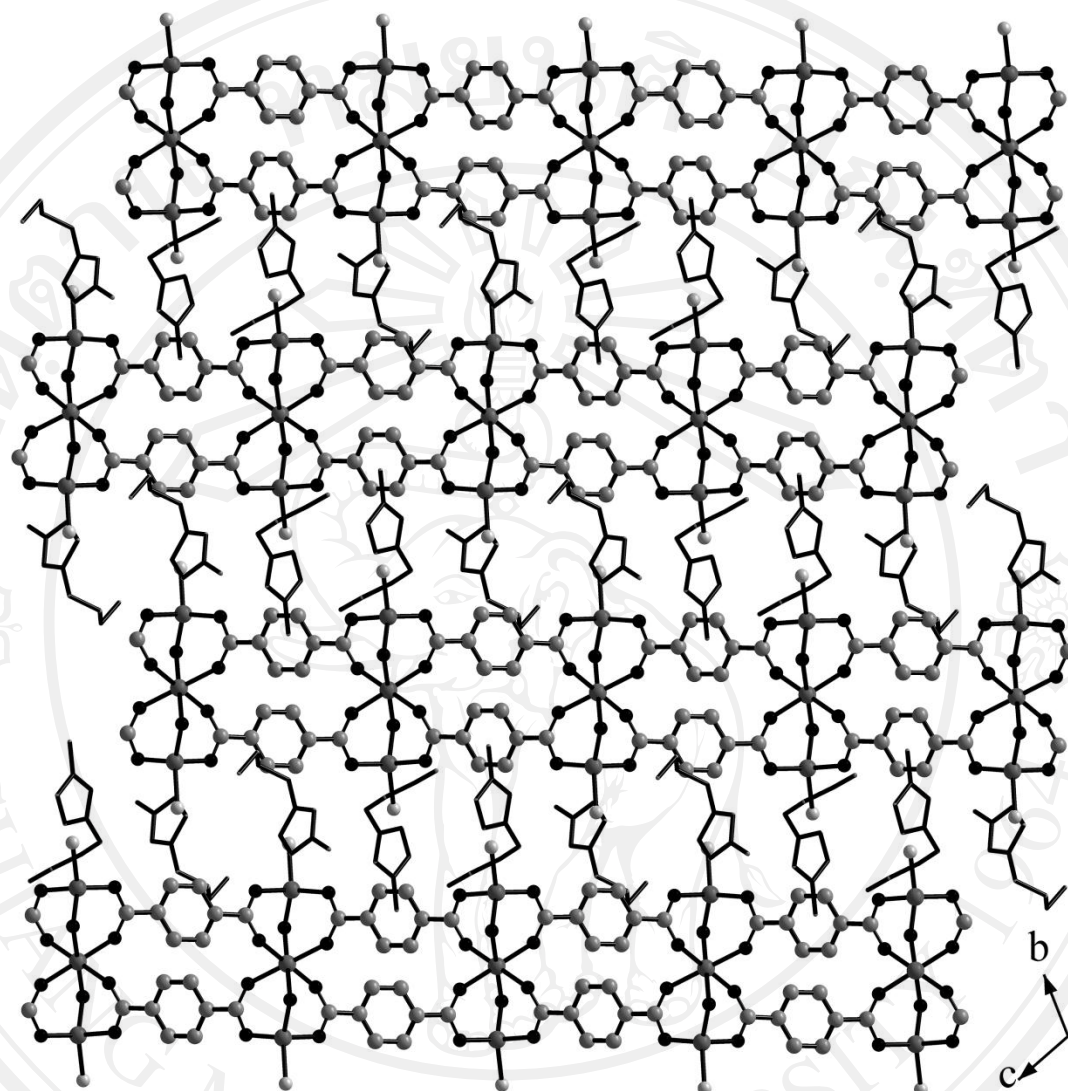


Fig. 5.5 The ABAB stacking of the two-dimensional in **V**, intercalated by the extraframework BMIm^+ cations.

Both the EMIm^+ and BMIm^+ cations are arranged in such a way that the positive imidazolium ring is oriented toward the electronegative Cl^- and the hydrocarbon tail toward the benzene ring of the BDC^{2-} ligand. This is clearly manifested in the case of the structure **V** in which the terminal methyl group of the BMIm^+ hydrocarbon chain involves in the $\text{C-H}\cdots\pi$ interaction with the phenyl ring of

the $\mu_2\text{-}\eta^1:\eta^1$ BDC²⁻ ligand; C32–H37A $\cdots\pi$ (C17–C18–C19–C10–C11–C20), $d = 2.986$ Å, $\angle = 155.08^\circ$ [30]. Although there is no evidence for the C–H $\cdots\pi$ interactions in **IV**, the spatial arrangement of the imidazolium ring of the EMIm⁺ cation affords the very weak C–H \cdots O hydrogen bonding interactions (Fig. 5.2a); C11–H10 \cdots O2 { $d(\text{C}\cdots\text{O}) = 3.21(1)$, $\angle(\text{CHO}) = 130.04^\circ$ } and C15–H20 \cdots O1 { $d(\text{C}\cdots\text{O}) = 3.32(2)$, $\angle(\text{CHO}) = 146.21^\circ$ }, as detailed in Table 5.6.

Table 5.6 Details of the hydrogen bonding interactions in **IV**. A hydrogen bond donor and acceptor are defined as D and A, respectively.

D–H \cdots A ^a	D–H, (Å)	H \cdots A, (Å)	D \cdots A, (Å)	D–H \cdots A, (°)
C11–H10 \cdots O2 ⁱ	0.9300	2.5290	3.208(11)	130.04
C15–H20 \cdots O1	0.9300	2.5042	3.317(15)	146.21

^a Symmetry code: (i) 2 - x, - y, - z.

The presence of these hydrogen bonding interactions presumably account for the better compact sheet structure of **IV**. The subtle difference in supramolecular interactions between the structures **IV** and **V** is apparently a principle reason for the refined variations in the sheet structures and inter-sheet distances between the two structures. The templating function of the ionic liquids is therefore illustrated.

The FT–IR (Fig 5.6) and Raman (Fig. 5.7) spectroscopic studies on compounds **IV** and **V** provide corresponding results to the single crystal studies. Lists of characteristic vibrations featuring different functional groups in the crystal structures of **IV** and **V** are summarized in Table 5.7.

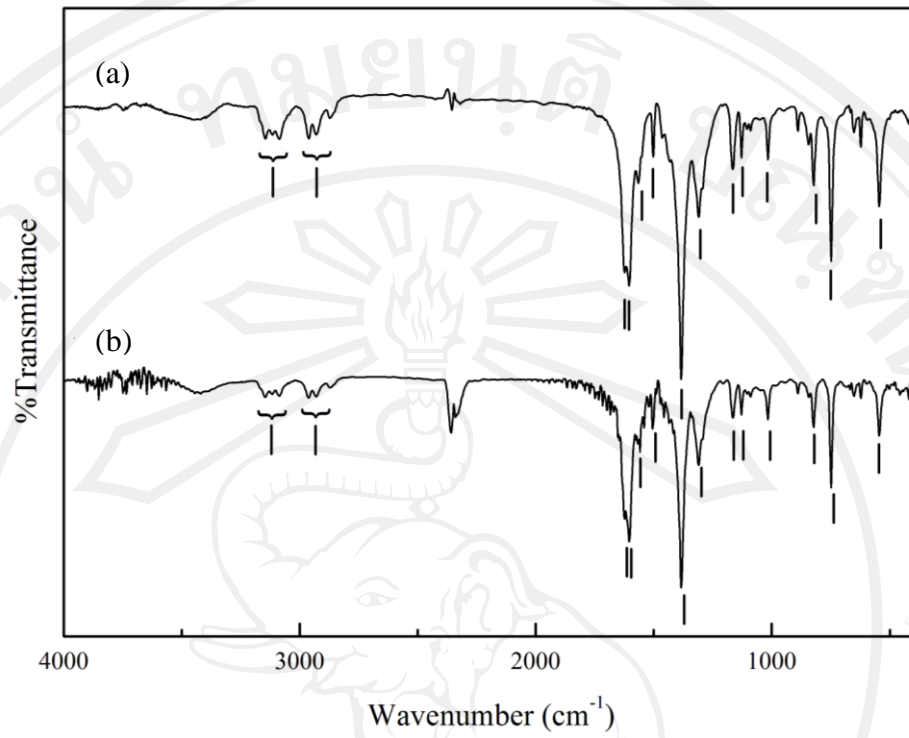


Fig. 5.6 FT-IR spectra of (a) IV and (b) V.

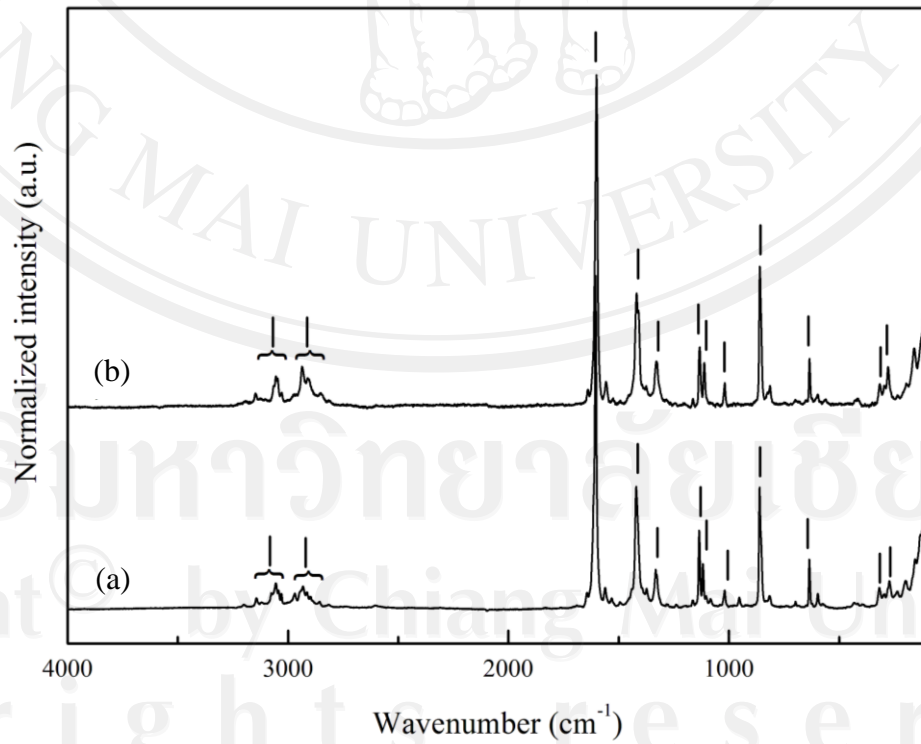


Fig. 5.7 Raman spectra of (a) IV and (b) V.

Table 5.7 FT-IR and Raman assignments for **IV**, **V**, **IV-L** and **V-L**.

Vibrational modes	IV		IV-L		V		V-L	
	IR	Raman	IR	Raman	IR	Raman	IR	Raman
v (Zn-O)	545	860	576	872	545	860	–	872
v (Zn-Cl)	–	278	–	286	–	278	–	287
v (O-H)	–	–	3248	–	–	–	3250	–
v _s (COO)	1385	1420	1383	1400	1383	1420	1385	1403
v _{as} (COO)	1566, 1604	1600	1577, 1651	1605	1558, 1604	1600	1581, 1651	1604
v (C-H), aliphatic	2872–2960	2856–2970	–	–	2870–2960	2850–2970	–	–
δ (C-H), aliphatic	1502	1332	–	–	1506	1330	–	–
v (C-H), aromatic	3086–3145	3030–3143	–	3040–3080	3086–3148	3029–3147	–	3040–3082
δ (C-H), aromatic	1016 (<i>ip.</i>) 1130 (<i>ip.</i>) 748 (<i>oop.</i>)	1135	1015 (<i>ip.</i>) 1148 (<i>ip.</i>) 748 (<i>oop.</i>)	1127	1016 (<i>ip.</i>) 1130 (<i>ip.</i>) 748 (<i>oop.</i>)	1132	1015 (<i>ip.</i>) 1148 (<i>ip.</i>) 748 (<i>oop.</i>)	1128
para-disubstitution	821	635	854	632	821	635	854	633
v (N-C), alkyl	1166	–	–	–	1164	n/a	–	–
v (C=N), imidazole	1624	1600	–	–	1624	1600	–	–
v (C-N), imidazole	1310	–	–	–	1310	n/a	–	–
v (C-C), aromatic	–	1019	–	–	n/a	1019	–	1017
v (C-C), aliphatic	–	1118	–	–	n/a	1112	–	–
δ (C-C), aliphatic	–	318	–	–	n/a	316	–	–

5.2.2 Thermogravimetric analysis

As clearly illustrated in Fig. 5.8, both compounds **IV** and **V** were thermally stable up to over 300 °C, after which a drastic weight loss of approximately 78–79% in total were observed for both compounds suggesting a decomposition of the structures. The remaining white residue is ZnO powder. A difference of 30 °C in the decomposing temperatures of compounds **IV** (370 °C) and **V** (340 °C) is worth noted. The better thermal robustness of compound **IV** may attribute to the better compact sheet structure.

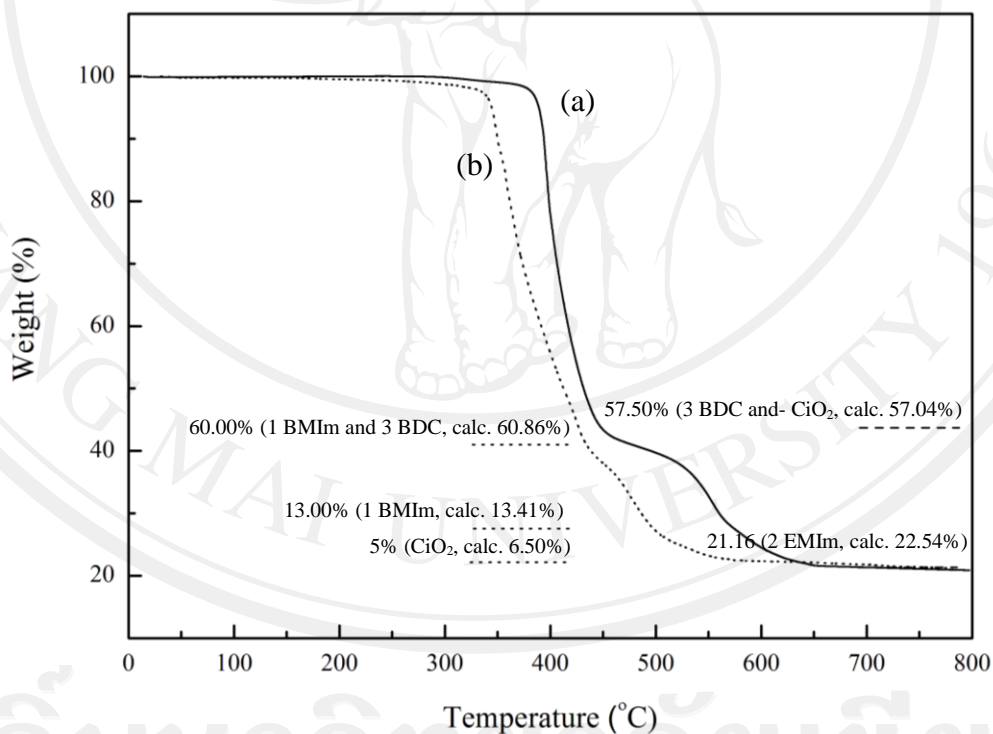


Fig. 5.8 Thermogravimetric curve collected on the ground crystals of (a) **IV** and (b) **V**.

5.2.3 UV–Vis and photoluminescent spectroscopic studies

The UV–Vis spectra of compounds **IV** and **V** compared with those of the ionic liquid and H₂BDC are shown in Fig. 5.9 and 5.10, respectively. Both compounds show two absorptions featuring at 240 and 288 nm, which can be assigned to the ligand-centered $\pi \rightarrow \pi^*$ and $n \rightarrow \pi^*$ transitions, respectively. The red shift in both features are vivid, and should attribute to the coordination of the BDC²⁻ to the metal ions. The retaining of the $n \rightarrow \pi^*$ transition in the spectra corresponds well with the presence of free carboxylato arms of the ligated BDC²⁻ in both compounds. The band gap energy of *ca.* 4.6 eV can be estimated for the $\pi \rightarrow \pi^*$ transition. This value was estimate from the *x*-axis intercept of the linear portion of a plot of $(\alpha hv)^2$ versus (hv) , where α is the absorption coefficient and hv is photon energy, as illustrated in Fig. 5.11. The α value obtained from the equation of $\alpha \cdot v = 2.303A/t$, where *A* is the absorbance and *t* is thickness or path length in the case of suspension sample [31]. The details of band gap energy determination by using the Tauc method are provided in Appendix B. At room temperature, the ground crystals of **IV** and **V** exhibit the blue emission with the excitation of 365 nm. Fig. 5.12 shows photoluminescence spectra of compounds **IV** and **V** compared to that of the H₂BDC with the excitation at 255 nm, affirming the blue luminescence to originate from the ligand–centered charge transfer process. The absence of ligand–to–metal charge transfer should be due to the fully occupied *d* orbitals (d^{10}) of Zn^{II} ions which in turn forbid a reduction at the metal site [4, 32, 33]. The retaining of the blue luminescence properties of the BDC²⁻ ligand in the thermally robust compounds may be worth noted.

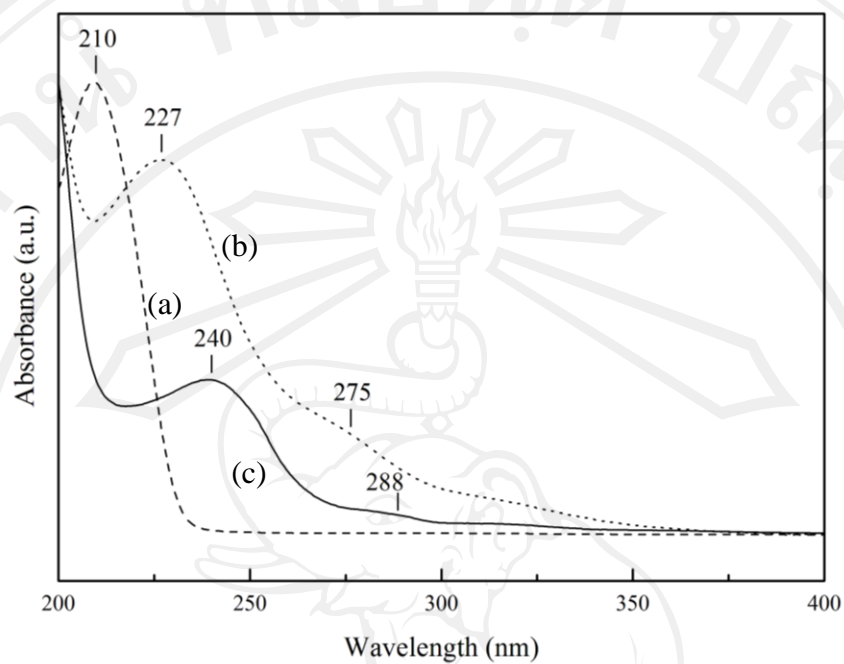


Fig. 5.9 UV-Vis spectra of (a) EMIm-Cl, (b) H₂BDC and (c) IV.

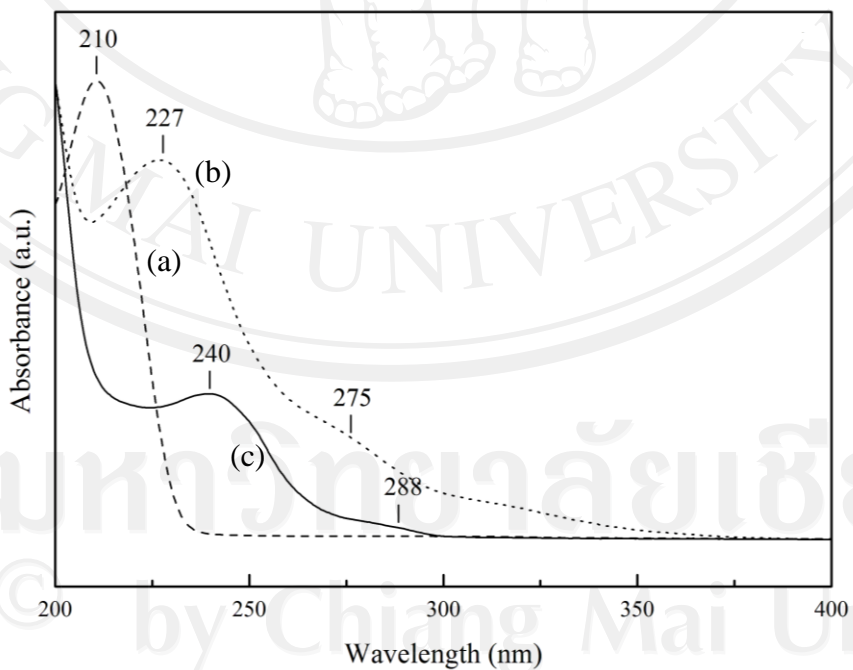


Fig. 5.10 UV-Vis spectra of (a) BMIm-Cl, (b) H₂BDC and (c) V.

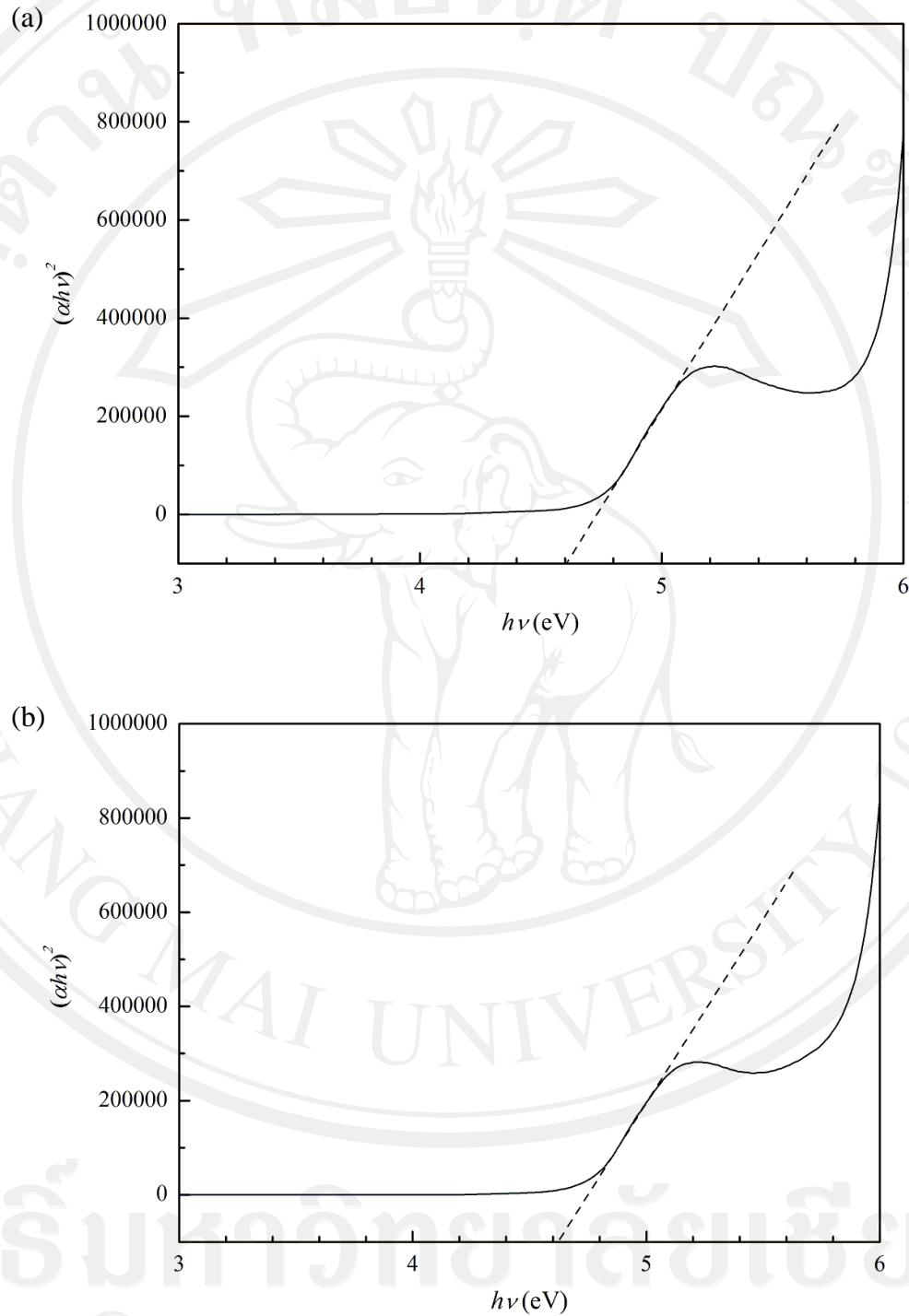


Fig. 5.11 Plots of $(\alpha h\nu)^2$ value versus photon energy ($h\nu$) for (a) **IV** and (b) **V**.

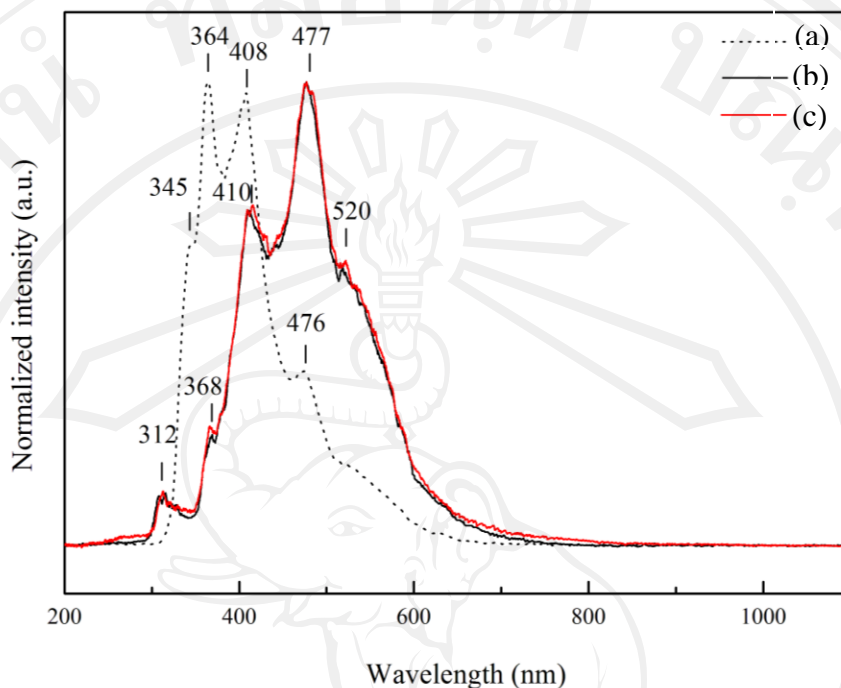


Fig. 5.12 Photoluminescent spectra of (a) H_2BDC , (b) **IV** and (c) **V**.

5.2.4 Stability and photoluminescence property of the de-intercalated **IV-L** and **V-L**

The importance and potential in industrial applications and advanced technology of materials with two-dimensional layered structures, particularly layered double hydroxides [34] and clays [35], are well recognized. Compounds **IV** and **V** with the cationic intercalated anionic layered structures may be a good candidate in this regard.

The powder X-ray diffraction patterns (Fig. 5.13 and 5.14) of the fine white powders **IV-L** and **V-L** yielded from the de-intercalation experiments of crystals **IV** and **V**, suggest the powders to be polycrystalline. The structures of the yielded **IV-L** and **V-L** however differ from those of **IV** and **V**, although characteristic of the layered structure is still apparent in the diffraction patterns; most intense peaks at 2θ of 7.45° and 7.31° .

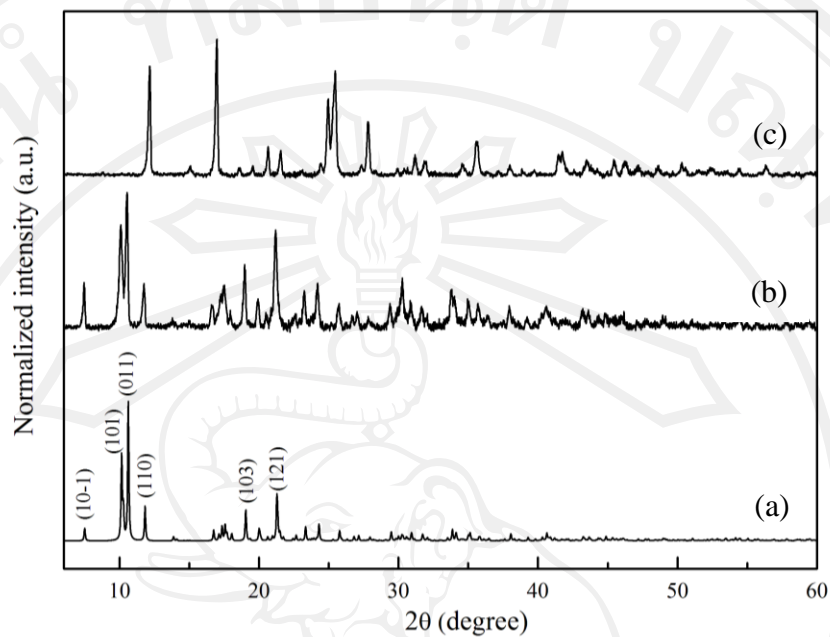


Fig. 5.13 PXR D patterns calculated from single crystal data of (a) **IV** compared with those collected on the bulk samples of (b) **IV** and (c) the de-intercalated **IV-L**.

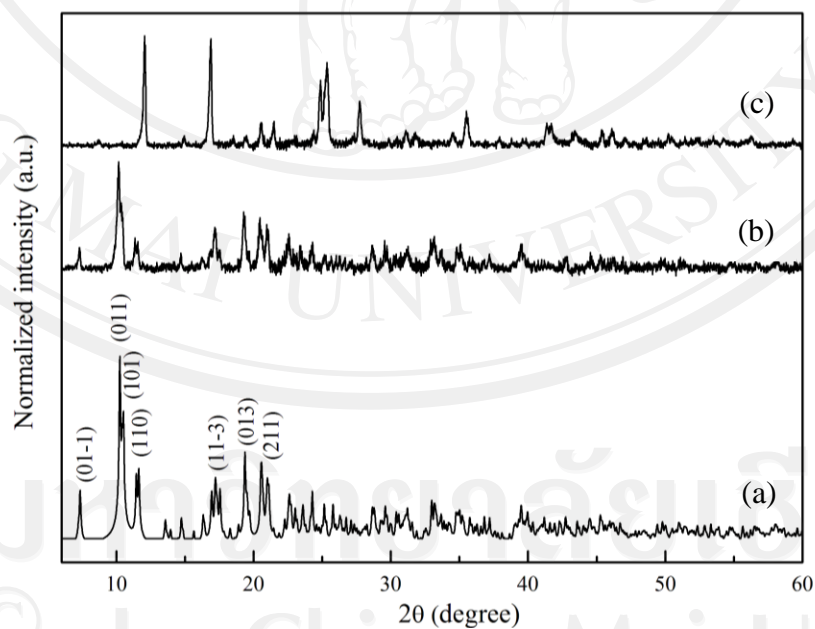


Fig. 5.14 PXR D patterns calculated from single crystal data of (a) **V** compared with those collected on the bulk samples of (b) **V** and (c) the de-intercalated **V-L**.

The elemental analyses results for **IV-L** (C, 36.42%; H 3.06%) and **V-L** (36.25%; H 3.00%) are notably the same, indicating an absence of nitrogen, which is in good agreement with the interpretations of the vibrational spectra (Fig. 5.15 and 5.16) of the two samples, as summarized in Table 5.7. The characteristic vibrations attributed to aliphatic hydrocarbon and imidazolium ring of the intercalated EMI⁺ and BMIm⁺ cations, *e.g.* $\nu(\text{C-H aliphatic})$, $\nu(\text{C-C aliphatic})$ and $\delta(\text{C-H aliphatic})$, which are clearly apparent in the spectra of **IV** and **V**, cannot be observed in the spectra of **IV-L** and **V-L**. It can therefore be concluded that the intercalated cations were liberated from **IV** and **V** during the de-intercalation experiments. The retaining of the $\nu(\text{Zn-O})$, $\nu(\text{Zn-Cl})$ and the other characteristic vibrations of the BDC²⁻ ligand nonetheless suggest the maintenance of the coordination of BDC²⁻ to the Zn ions.

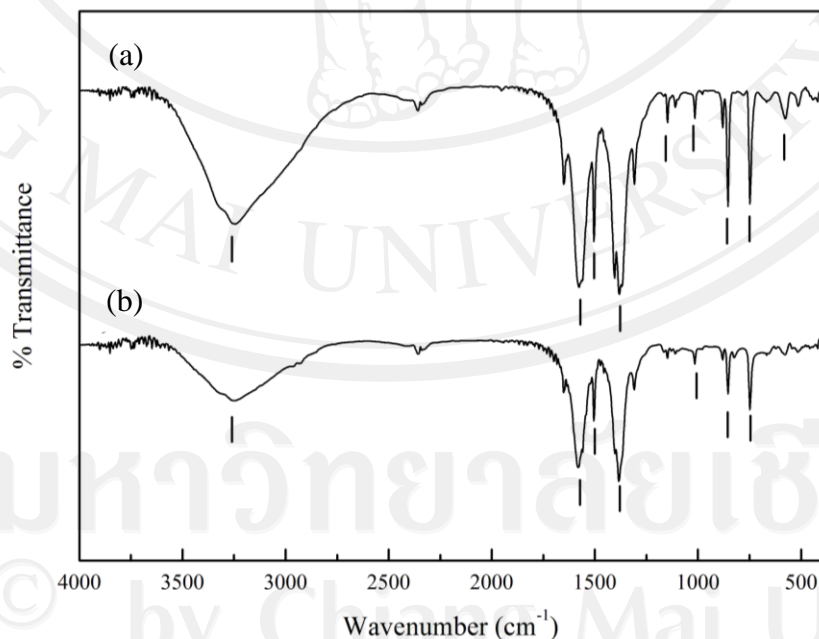


Fig. 5.15 FT-IR spectra of the de-intercalated (a) **IV-L** and (b) **V-L**.

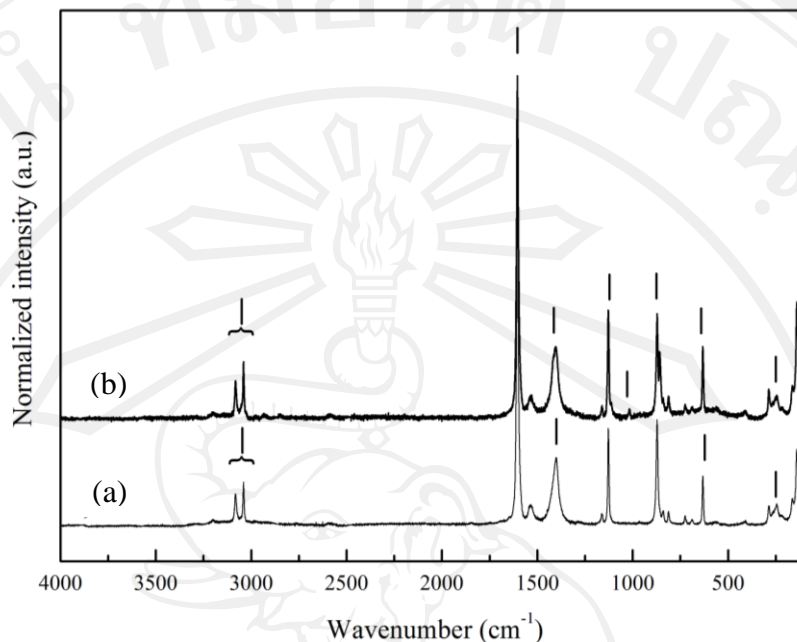


Fig. 5.16 Raman spectra of the de-intercalated (a) **IV-L** and (b) **V-L**.

In addition, the presence of the intense and broad band in a range of 3000–3500 cm^{-1} for the IR spectra of **IV-L** and **V-L** suggests the absorption of the water molecules by the two samples. This is affirmed by the thermogravimetric analyses, as depicted in Fig. 5.17. The weight loss patterns in **IV-L** and **V-L** are similar and different from those of **IV** and **V**. There are two weight losses in the thermogravimetric curve of **IV-L** and **V-L**, including the first loss in a temperature range 100–200 $^{\circ}\text{C}$ attributing to the loss of crystallizing water, and the second abrupt loss in a range 450–500 $^{\circ}\text{C}$ contributing to the decomposition of the two-dimensional structure. The decomposing temperature for **IV-L** and **V-L** is *ca.* 50 $^{\circ}\text{C}$ higher than those of **IV** and **V**. The preserve of the blue luminescence for **IV-L** and **V-L**, when being excited at the same wavelength as **IV** and **V**, is shown in Fig. 5.18.

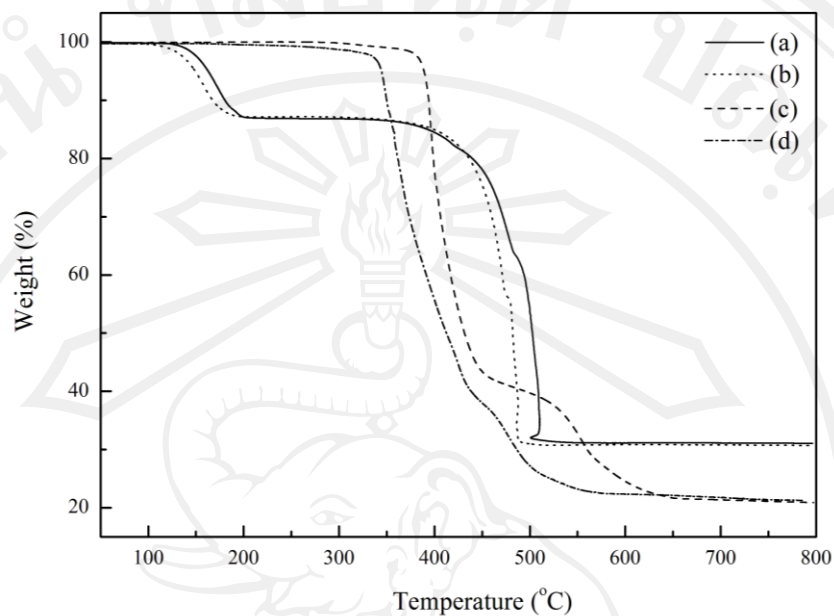


Fig. 5.17 Thermogravimetric curves of the de-intercalated (a) **IV-L** and (b) **V-L**, compared with those of the prior de-intercalated (c) **IV** and (d) **V**, respectively.

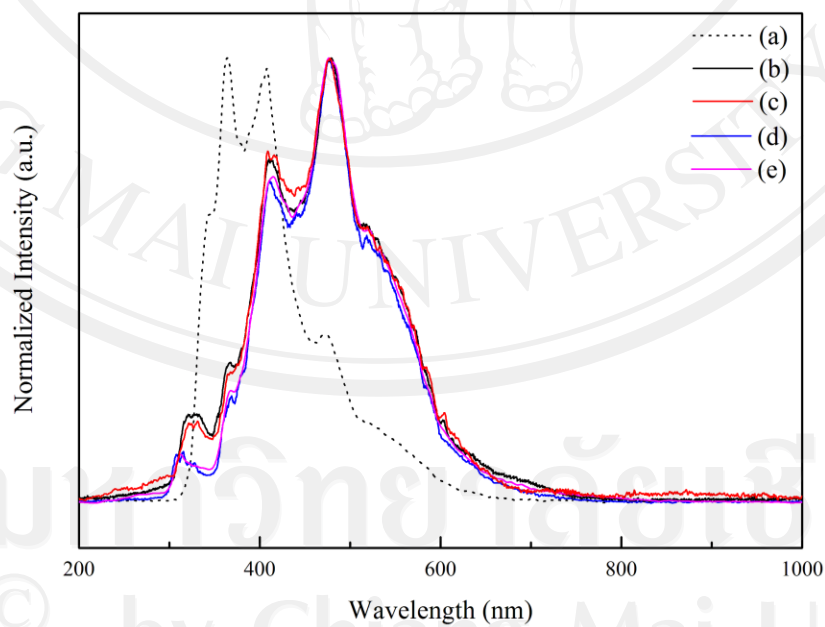


Fig. 5.18 Photoluminescent spectra of (a) H_2BDC , the de-intercalated (b) **IV-L** and (c) **V-L**, compared with those of the prior de-intercalated (d) **IV** and (e) **V**, respectively.

While this affirms the origin of the blue luminescence to be from the BDC^{2-} ligand-centered $\pi \rightarrow \pi^*$ and $n \rightarrow \pi^*$ transitions, similarities in the band profile of these spectra suggest the maintenance of the local environment of the BDC^{2-} ligand in the 2-D structure of **IV-L** and **V-L**.

5.3 Conclusions

In summary, two new d^{10} coordination polymers $\text{EMIm}_2[\text{Zn}_3(\text{BDC})_3\text{Cl}_2]$ (**IV**) and $\text{BMIm}_2[\text{Zn}_3(\text{BDC})_3\text{Cl}_2]$ (**V**) were synthesized under ionothermal conditions, and fully characterized. The compounds feature the same isorecticular $[\text{Zn}_3(\text{BDC})_3\text{Cl}_2]^{2-}$ anionic layered structure of 3^6hxl topology, which is intercalated by the extraframework cations, *i.e.* EMIm^+ (**IV**) and BMIm^+ (**V**), derived from the ionic liquid reaction medium. Despite the same chemical composition meaning the same $[\text{Zn}_3\text{O}_2(\text{OCO})_4\text{Cl}_2]$ building motifs and the BDC^{2-} bridging patterns, subtle differences in the sheet structure and supramolecular interactions are apparent. This consequently imparts the effect on the refined difference in thermogravimetric properties of the two compounds. Because of d^{10} configuration of the Zn ions, the optical spectroscopic properties including the blue luminescence of **IV** and **V** originates principally from the BDC^{2-} ligand. The de-intercalation experiments of **IV** and **V** have been performed and resulted in the better thermally robust two-dimensional structures (**IV-L** and **V-L**), comprising presumably similar Zn-BDC coordination networks as **IV** and **V**. The de-intercalation of the extraframework EMIm^+ and BMIm^+ cations is affirmed by vibrational spectroscopy. The maintenance of blue luminescence properties in **IV-L** and **V-L** with similar band profile to those of **IV** and **V**

supports the postulation that the optical spectroscopic properties originate principally from the BDC²⁻ ligand. The significant thermal stability and robustness toward the de-intercalation of these blue luminescence compounds imply the compounds to be a great candidacy for further investigation on potential applications.

REFERENCES

1. H. Li, M. Eddaoudi, M. O'Keeffe, O. M. Yaghi, *Nature*, 402 (1999) 276.
2. R.J. Kuppler, D.J. Timmons, Q.-R. Fang, J.-R. Li, T.A. Makala, M.D. Young, D. Yuan, D. Zhao, W. Zhuang, H.-C. Zhou, *Coord. Chem. Rev.* 253 (2009) 3042.
3. A.Y. Robin, K.M. Fromm, *Coord. Chem. Rev.* 250 (2006) 2127.
4. S. Huh, S. Jung, Y. Kim, S.-J. Kim, S. Park, *Dalton Trans.* 39 (2010) 1261.
5. J.L.C. Rowsell, O.M. Yaghi, *Microporous Mesoporous Mater.* 73 (2004) 3.
6. S. Natarajan, P. Mahata, *Chem. Soc. Rev.* 38 (2009) 2304.
7. S. Choubey, S. Roy, K. Bhar, Rajarshi Ghosh, P. Mitra, C.-H. Lin, J. Ribas, B.K. Ghosh, *Polyhedron* 55 (2013) 1.
8. S. Qiu, G. Zhu, *Coord. Chem. Rev.* 253 (2009) 2891.
9. R.D. Rogers, K.R. Seddon, *Science* 302 (2003) 792.
10. E.R. Parnham, R.E. Morris, *Acc. Chem. Res.* 40 (2007) 1005.
11. R.E. Morris, *Chem. Commun.* (2009) 2990.
12. Z. Lin, D.S. Wragg, J.E. Warren, R.E. Morris, *J. Am. Chem. Soc.* 129 (2007) 10334.
13. L. Xu, E.-Y. Choi, Y.-U. Kwon, *Inorg. Chem.* 46 (2007) 10670.

14. J.-H. Liao, W.-C. Huang, *Inorg. Chem. Commun.* 9 (2006) 1227.
15. Z. Lin, D.S. Wragg, R.E. Morris, *Chem. Commun.* (2006) 2021.
16. J. Zhang, S. Chen, X. Bu, *Angew. Chem. Int. Ed.* 47 (2008) 5434.
17. C.N.R. Rao, S. Natarajan, R. Vaidhyathan, *Angew. Chem. Int. Ed.* 43 (2004) 1466.
18. M.E. Braun, C.D. Steffek, J. Kim, P.G. Rasmussen, O.M. Yaghi, *Chem. Commun.* (2001) 2532.
19. M. Eddaoudi, D.B. Moler, H. Li, B. Chen, T.M. Reineke, M. O’Keeffe, O.M. Yaghi, *Acc. Chem. Res.* 34 (2001) 319.
20. M. Eddaoudi, J. Kim, N. Rosi, D. Vodak, J. Wachter, M. O’Keeffe, O.M. Yaghi, *Science* 295 (2002) 469.
21. Bruker (2007). SAINT. Bruker AXS Inc., Madison, Wisconsin, USA.
22. Bruker (2001). SADABS. Bruker AXS Inc., Madison, Wisconsin, USA.
23. G.M. Sheldrick, *Acta. Cryst. A* 64 (2008) 112.
24. L.J. Farrugia, *J. Appl. Cryst.* 32 (1999) 837.
25. R.I. Cooper, R.O. Gould, S. Parsons, D.J. Watkin, *J. Appl. Cryst.* 35 (2002) 168.
26. S.M. Hawxwell, H. Adams, L. Brammer, *Acta. Cryst. B* 62 (2006) 808.
27. J. Sun, Y. Zhou, Q. Fang, Z. Chen, L. Weng, G. Zhu, S. Qiu, D. Zhao, *Inorg. Chem.* 45 (2006) 8677.
28. M. Edgar, R. Mitchell, A.M.Z. Slawin, P. Lightfoot, P.A. Wright, *Chem. Eur. J.* 7 (2001) 5168.

29. A.L. Grzesiak, F.J. Uribe, N.W. Ockwig, O.M. Yaghi, A.J. Matzger, *Angew. Chem. Int. Ed.* 45 (2006) 2553.
30. M. Nishio, Y. Umezawa, K. Honda, S. Tsuboyamad, H. Suezawa, *Cryst. Eng. Comm.* 11 (2009) 1757.
31. J. Tauc, *Amorphous and Liquid Semiconductors*, Plenum Press, London and New York, 1974.
32. V.W.–W. Yam, K.K.–W. Lo, *Chem. Soc. Rev.* 28 (1999) 323.
33. I. Britoa, J. Vallejosa, A. Cárdenasb, M.L. Rodríguezc, M. Bolted, J. Llanose, *Inorg. Chem. Commun.* 14 (2011) 897.
34. Z.P. Xu, J. Zhang, M.O. Adebajo, H. Zhang, C. Zhou, *Appl. Clay Sci.* 53 (2011) 139.
35. C.H. Zhou, J. Keeling, *Appl. Clay Sci.* 74 (2013) 3.